Structural, Optical, and Multiferroic Properties of Yttrium (Y^{3+})-Substituted BiFeO$_3$ Nanostructures

Nidhi Sheoran[1] · Ashok Kumar[1] · Vinod Kumar[1] · A. Banerjee[2]

Abstract

Nanoparticles of Bi$_{1-x}$Y$_x$FeO$_3$ ($x = 0.0, 0.1, 0.15, 0.2$) were synthesized by sol-gel pursued auto-combustion route. X-ray diffraction (XRD) pattern was recorded for analysis of the phase formation of pristine BiFeO$_3$ (BFO) and Y^{3+}-substituted samples. A systematic decrease in crystallite size with increasing concentration of Y^{3+} was observed by XRD and W-H plot. FESEM micrograph demonstrated clearly that the average grain size is decreased with increasing Y^{3+} ion concentration. Compositional analysis was carried out by EDS. Optical properties of the developed nanoparticles were examined by diffuse reflectance spectroscopy; it is observed that optical band gap decreases with increase in Y^{3+} ion concentration. Vibrating sample magnetometer (VSM) analysis revealed weak ferromagnetic behavior for pristine BFO. The ferromagnetic behavior has been enhanced with increasing concentration of Y^{3+} ions in BFO. Temperature dependence of dielectric constant shows an anomaly near the antiferromagnetic transition temperature in the developed materials that revealed the existence of magnetoelectric coupling in all the samples. Improved ferroelectric property has been observed by virtue of enhancement in the polarization of all substituted samples. Variation of electric field–guided strain with applied electric field has shown asymmetric behavior for samples $x \leq 0.15$ and symmetric loop has been observed for $x = 0.2$ with the highest peak to peak strain value which makes it active material for electronic and magnetic devices.

Keywords Nanoparticles · Structural transformation · Multiferroic · Magnetization · Polarization

1 Introduction

Devices such as actuators, sensors, spintronics, and magnetic recording media can be developed and improved by using multiferroic materials that controlled all electric, magnetic, and elastic orders together. These multiferroic materials have also been renovated, by virtue of its additional functionalities that occur due to other possible magnetic and electric dipole interactions [1]. One of them is bismuth ferrite (BFO) having distorted rhombohedral perovskite structure with R3c space group and the only single-phase multiferroic material which has a G-type antiferromagnetic order below Neel temperature ($T_N \sim 370$ °C) and high ferroelectric Curie temperature

($T_C \sim 830$ °C) that encourage its magnetoelectric coupling property at and above room temperature [2–4]. Further, the ferroelectric behavior in BFO is emerged due to the movement of Bi^{3+} ions lone pair electrons in 6s^2 orbital and Fe^{3+} ions with respect to [111] direction. While magnetic behavior is arisen as a result of partially filled d orbital of Fe ions that give G-type antiferromagnetic ordering via magnetic exchange interaction through O^{2-} along with Dzyaloshinskii-Moriya (D-M) interaction origin of feeble ferromagnetism [5–7]. Thus, BFO continuously get consideration of scientific communities due to its special characteristics along with the weak ferromagnetic behavior at room temperature for possible applications in sensors, data storage, spintronic devices, photovoltaic facilities, and photocatalysts [8, 9]. Also, the appropriate band gap of BFO (~2.2 eV) makes it a promising material for photovoltaic, sola cell, and photocatalytic applications [10]. Magnetoelectric coupling in BFO can be enhanced by decreasing the particle size smaller than the spin spiral structure of wavelength ~ 64 nm that prevent the net magnetization [7, 11, 12]. Pure phase synthesis of BFO is still problematic due to its formation kinetics that grows two

✉ Vinod Kumar
  vinod.phy@dcrustm.org

1 Department of Physics, Deenbandhu Chhotu Ram University of Science and Technology, Murthal, Haryana 131039, India

2 UGC-DAE Consortium for Scientific Research, Indore, M.P. 452001, India

impurity phases such as $Bi_2Fe_4O_9$ (mullite) and $Bi_{25}FeO_{39}$ (sillenite) [7]. These impurity phases may increase leakage current that limit its use for device application [13, 14]. The various approaches were endorsed to curtail the leakage current and advancement in multiferroic properties of BFO such a synthesis of nanosized BFO by different synthesis route (sol-gel, hydrothermal, coprecipitation, and solid state methods) and lattice site substitution in BFO with convenient elements/ions [15–17]. Moreover, yttrium-substituted bismuth ferrite nanoparticles with enhanced multiferroic and optical properties with respect to the BFO nanoparticles have been reported earlier [10, 18–20]. In the present work, we have synthesized yttrium (Y^{3+})-substituted BFO nanoparticles through sol-gel auto-combustion route. This method is most appropriate due to its low-temperature synthesis route than high-temperature use in solid state method. Also for composition $x = 0.1$ to 0.15 R3c phase is maintained and for $x = 0.2$, there is phase transformation that are consistent with previous XRD results of Gautam et al. [20]. Moreover, we explore together all structural, optical, magnetic, ferroelectric, and dielectric properties of $Bi_{1-x}Y_xFeO_3$ ($x = 0.0$, 0.1, 0.15, 0.2) nanoparticles, which is less reported earlier for this composition.

2 Experimental Section

2.1 Synthesis of $Bi_{1-x}Y_xFeO_3$ Nanoparticles

$Bi_{1-x}Y_xFeO_3$ ($x = 0.0, 0.1, 0.15, 0.2$) nanoparticles were developed by low-temperature sol-gel auto-combustion route as shown in Fig. 1a. The precursor solutions were processed using the stoichiometric amount of raw materials Bi $(NO_3)_3 \cdot 6H_2O$ (bismuth nitrate hexahydrate), $Fe(NO_3)_3 \cdot 9H_2O$ (ferric nitrate nonahydrate), and $Y(NO_3)_3 \cdot 6H_2O$ (yttrium nitrate hexahydrate) of Sigma Aldrich, purity > 99%. Firstly, the stoichiometry amount of bismuth nitrate was dissolved in distilled water and 2 ml nitric acid and next iron nitrate were added to it with regular stirring to get a well-homogeneous solution.

After that citric acid was added in a 1 : 1 ratio of metal ions as a chelating agent under continuous constant stirring for 2 h. Then, the procured light brown solution was heated at a temperature of 80 °C till it became gel. During continuous heating on hot plate, dried paste auto-ignited and liberated huge amount of gases and finally, xerogel powder was obtained. Then, the powder was ground in the mortar pestle and thus obtained nanoparticles were annealed at 600 °C for 4 h. Further, dense pellets of thickness 1.5 mm and diameter 10 mm were obtained with the help of the hydraulic press and painted with silver paste for electrical characterization.

## 2.2 Instrumentation Specifications

The phase architecture of developed nanoparticles was analyzed through X-ray diffraction technique by operating Rigaku Ultima IV equipped with CuKα radiation (1.5406 Å). Field emission scanning electron microscopy (FESEM) (Nova Nano FE-SEM 450) assembled with energy dispersive spectroscopy (EDS) and operating acceleration voltage of 15 kV was regulated to obtain morphology and compositional analysis of samples. A UV-visible diffuse reflectance spectrum (PerkinElmer Lambda 1050) was used to determine the optical properties of developed samples. Room temperature magnetic measurement was carried out by vibrating sample magnetometer (Lakeshore Model 7400) applying a magnetic field range of ± 17 kOe. Impedance analyzer operated in frequency range 20 Hz–1 MHz (Wayne Kerr-6500B) has been used for dielectric measurements. Automatic P-E Loop Tracer (Marine India) was used to perform ferroelectric measurements.

3 Results and Discussion

3.1 XRD Analysis

The phase analysis of the developed $Bi_{1-x}Y_xFeO_3$ ($x = 0.0, 0.1,$ $0.15, 0.2$) composition is analyzed via X-ray diffraction pattern which is depicted in Fig.1. Observed peak in the XRD pattern for samples ($x = 0.0, 0.1, 0.15, 0.2$) are well indexed to perovskite structure (JCPD 01-072-7678), and for $x = 0.2$, the number of peaks are significantly changed and also, peak splitting disappeared that represent large structural distortion which is consistent with the earlier results [18]. Some impurity peaks distinct by *$Bi_2Fe_4O_9$ formed dominantly during the synthesis process because of the volatile nature of bismuth at increasing temperature. But, it was noticed in the X-ray diffraction results that the secondary phase has been reduced in the doped samples; however, the effect is small for samples with lower doping compositions and extra phase removal has been clearly seen in samples with compositions $x = 0.2$. The lattice parameters and unit cell volume obtained from Fig. 1 are displayed in Table 1. The observed lattice parameter and unit cell volume are decreases by increasing Y^{3+} concentration into BFO lattice. The observed value of lattice parameters for $x \leq 0.15$ revealed small structure transformation and significant transformation is observed for $x = 0.2$ composition. As the radius of Y^{3+}(1.02 Å) is smaller than Bi^{3+} (1.17 Å) which may be responsible for the decrease in lattice parameter and unit cell volume. Consequently, structural transformation occurs due to mismatch of ionic radii of Y^{3+} and Bi^{3+} ions [21]. Further, the average crystallite size (δ) was calculated by the Debye-Scherrer equation:

Fig. 1 **a** Schematic diagram of synthesis of $Bi_{1-x}Y_xFeO_3$ ($x = 0.0$, 0.1, 0.15, 0.2) nanoparticles by Sol-gel auto combustion route. **b** XRD pattern of $Bi_{1-x}Y_xFeO_3$ ($x = 0.0$, 0.1, 0.15, 0.2) nanoparticles at room temperature
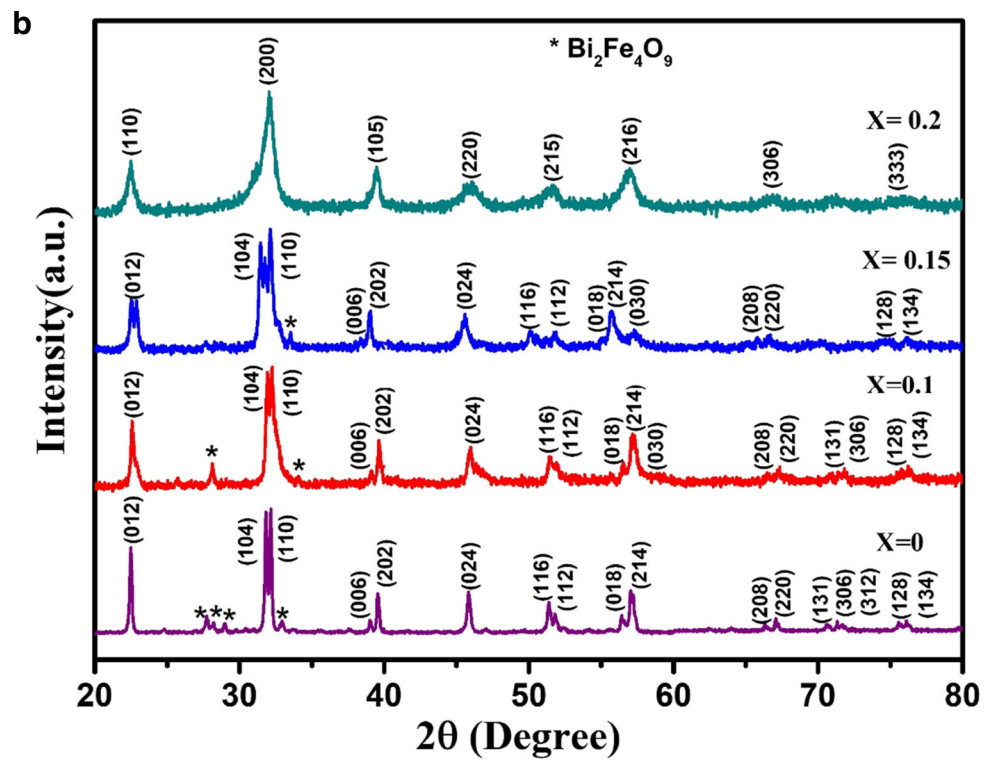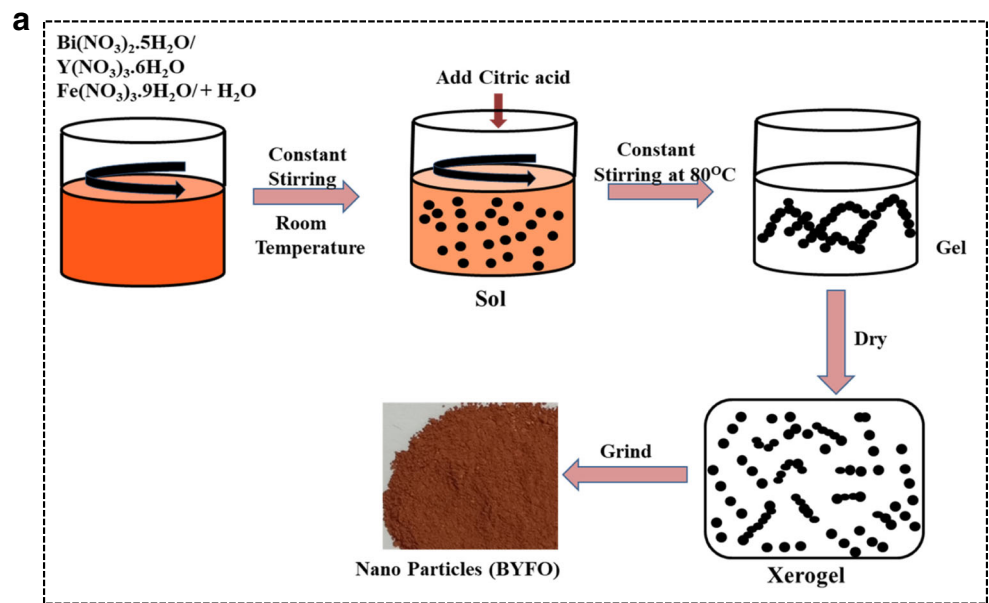
$$\delta = \frac{k\lambda}{\beta \cos\theta} \quad (1)$$

where k is the symbol for shape factor having a value 0.9, λ is the X-ray wavelength, peak position is determined by θ, and β stands for full-width at half-maxima for maximum intense peak. The estimated value of the average crystallite size is decreased by increasing Y^{3+} concentration which is shown in Table 1. The decreasing size with increasing concentration may be attributed to induced strain while synthesis or

difference in ionic radius of Y^{3+} (1.02 Å) and Bi^{3+} (1.17 Å). Moreover, we have followed the Williamson-Hall (W-H) approach to evaluate approximate confirmation about the crystallite size (τ) and microstrain (η) in the current samples. The W-H equation that connects the crystallite size (τ) and induced microstrain (η) together is represented by

$$\beta \cos\theta = \frac{k\lambda}{\tau} + 4\eta \sin\theta \quad (2)$$

Table 1 Crystallite size (calculated by Debye-Scherrer and W-H method), lattice parameters, volume (V), lattice strain (η), tolerance factor (t), and grain size obtained by FESEM micrograph of $Bi_{1-x}Y_xFeO_3$ (x = 0.0, 0.1, 0.15, 0.2) nanoparticles

Sample	Crystallite size (nm)		Lattice Parameters		Volume, V (Å)^3	Micro-strain (η)	Tolerance factor (t)	Grain size (nm)
	Debye-Scherrer method, δ (nm)	Williamson-Hall method, τ (nm)	$a = b$ (Å)	c (Å)				
x = 0.0	65	79 ± 0.3	5.710	13.80	389	0.0032	0.832	122
x = 0.1	55	75 ± 0.2	5.567	13.85	372	0.0034	0.827	90
x = 0.15	45	62 ± 0.4	5.563	13.82	370	0.0042	0.825	64
x = 2.0	17	25 ± 0.5	5.552	12.47	334	0.0062	0.822	41

The graph has been plotted between $4\sin\theta$ (x-axis) and $\beta\cos\theta$ (y-axis) which is depicted in Fig. 2. Crystallite size (τ) and microstrain (η) were computed by intercept and slope of graph, respectively, that are tabulated in Table 1. Data points are far away from best-fitted line that represent uncertainties which can be shown by including error bar graphically. So, by using bar graph the true value of crystallite size (τ) has been

calculated which is shown in Table 1. Also, positive values of slope manifest the potentiality of tensile strain in the samples [22]. The variation has been observed between the values of crystallite size calculated by Debye-Scherrer and W-H method which is a direct consequence of the strain in the samples that may arise due to the incorporation of ferroelectric and ferromagnetic phase together [23].
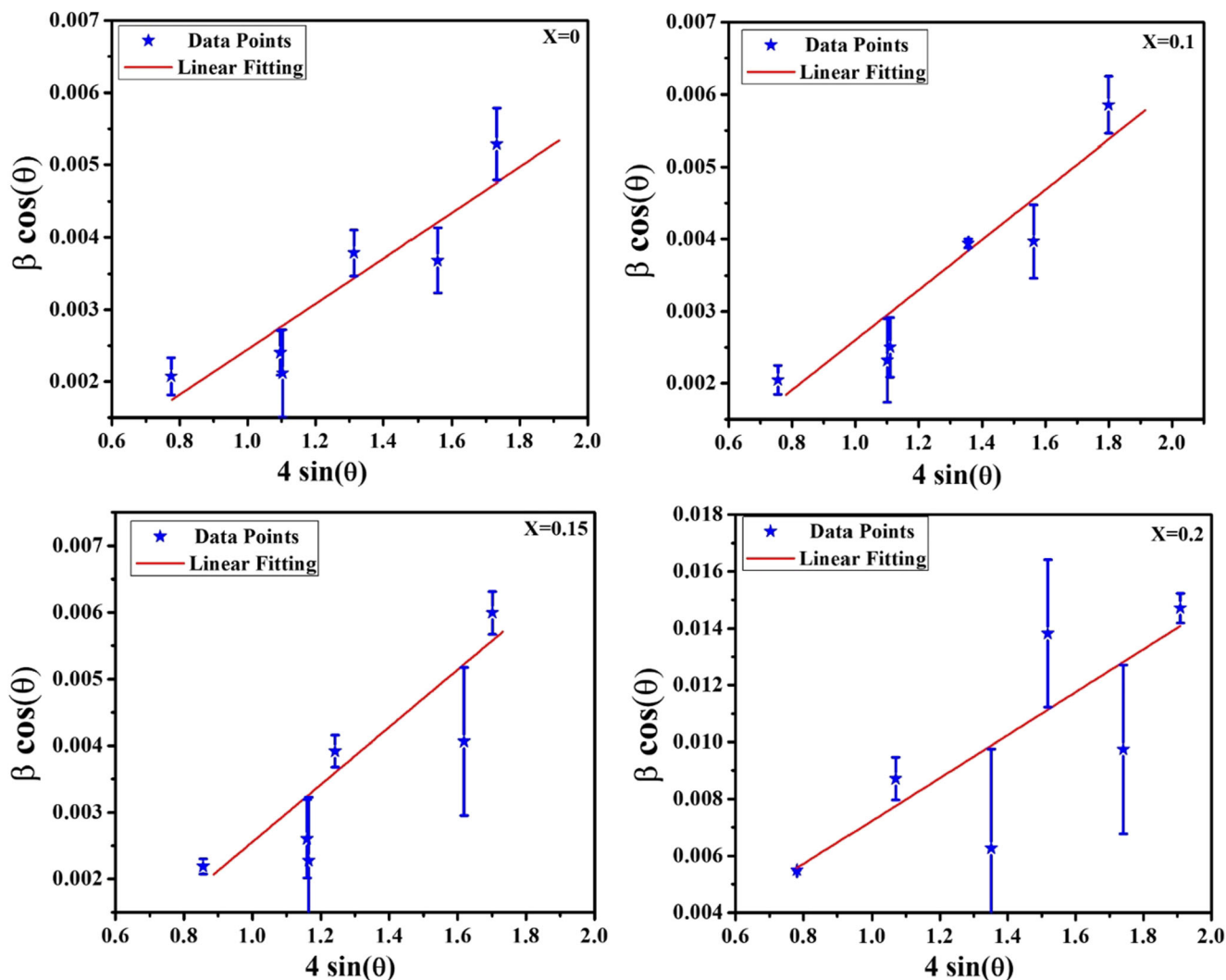
Fig. 2 Williamson-Hall (W-H) plots of $Bi_{1-x}Y_xFeO_3$ (x = 0.0, 0.1, 0.15, 0.2) nanoparticles

Further, the Goldsmith tolerance factor (t), which is defined for perovskite materials has been expressed for the current samples by an equation:

$$t = \frac{(1-x)r_{Bi^{3+}} + xr_{Y^{3+}} + r_{O^{2-}}}{\sqrt{2}(r_{Fe^{3+}} + r_{O^{2-}})} \tag{3}$$

where r is the ionic radius of respective elements and x is the concentration of doping element i.e., Y^{3+}. The estimated values of t decreases with progressive doping of Y^{3+} in BFO which are tabulated in Table 1. The decrease in value of t indicate structural transition due to an increase in oxygen octahedral tilting angle which is zero for ideal perovskite structure [24]. Also, the tolerance factor value $t = 1$ stands for ideal perovskite crystal and deviation of t from 1 or $t < 1$ pointed out strain produced associated with lattice imbalance. Thus, all developed samples having values $t < 1$ proposed that Bi/Y-O bond would be stretched and Fe-O bond intend to compress and transformation of the structure takes place beyond the distortion limit. Therefore, for sample $x = 0.2$ having value $t = 0.822$ large structure transformation take place as compared to other samples ($x = 0.0$ to 0.15).

3.2 Morphology and Composition Analysis

The morphological analysis of developed $Bi_{1-x}Y_xFeO_3$ ($x = 0.0, 0.1, 0.15, 0.2$) nanoparticles is accomplish via FESEM which is depicted in Fig. 3. In micrograph $x = 0.0$, the grain growth of BFO is not uniform and there is amalgamate of cubic/uneven morphology.

As we increase the doping concentration of Y^{3+}, there is little improvement in the homogeneity of the particles and it is worth mentioning that relatively spherical crystallite are present in the $x = 0.2$ sample. Also, the structure transformation is complete at this particular $x = 0.2$ concentration that supports the XRD results. Micrographs demonstrate clearly that as we increase the concentration of Y^{3+} the average grain size of developed nanoparticles decreases. The observed average grain size for $x = 0.0, 0.1, 0.15,$ and 0.2 are 122 nm, 90 nm, 64 nm, and 41 nm, respectively, are shown in Table 1 which is consistent with XRD results. Different size and shape of grains represent polycrystalline nature. Thus, doping of Y^{3+} in BFO play a vital role in reducing grain size and repress grain growth of BFO as recognized from FESEM micrograph depicted in Fig. 3. This reducing grain size may be due to the mismatch in ionic radius of Bi^{3+} (1.17 Å) and Y^{3+} (1.02 Å) [21]. The Kirkendall effect which occurs by virtue of diffusion rates of constituting elements of composition is also responsible for reducing grain size [25].

Figure 4 displayed the EDS spectra of all the compositions ($x = 0.0, 0.1, 0.15, 0.2$) to execute elemental analysis. All the requisite elements in the samples i.e., Bi, Fe, Y, and O has been designated by the EDS spectra that assure architecture of

BFO and Y-substituted BFO. And, no other extra peaks have been observed in all the spectra that confirm its phase purity.

3.3 Optical Analysis

The optical properties of bare and Y^{3+}-substituted bismuth ferrite nanoparticles were explored via UV-visible diffuse reflectance spectroscopy (DRS) spectra. Figure 5 displays the UV-vis DRS spectra of the developed $Bi_{1-x}Y_xFeO_3$ ($x = 0.0, 0.1, 0.15, 0.2$) nanoparticles having wavelength range of 300–800 nm. Now, in order to obtain absorption coefficient (α), these DRS spectra for all composition converted into Kubelka-Munk function [26]. All the samples perform broad range absorption in the visible region and absorption cut off wavelength in 600–650 nm range was observed. Further, the optical band gap (E_g) of all the nanoparticles are computed using Tauc's relation [27]:

$$(\alpha h \nu)^{1/n} = A(h\nu - E_g) \tag{4}$$

where ν is frequency, h is Planck's constant, A is constant of proportionality, and E_g represent optical band gap having unit electron-volt.

For $n = 1/2$, there will be direct band gap transition whereas $n = 2$ represent the indirect transition value. As for BFO, the band gap is direct; therefore, $n = 1/2$ is taken to calculate the energy band gap [28]. Now to estimate the value of E_g, graph is plotted by taking $(\alpha h \nu)^2$ as y-axis and $h\nu$ as x-axis, then extrapolating the linear region of $(\alpha h \nu)^2 \rightarrow 0$ gives directly the band gap value for all the composition ($x = 0.0, 0.1, 0.15, 0.2$) which is depicted in inset of UV-vis spectra graph of all respective composition. The observed value of E_g are 1.90, 1.85, 1.80, and 1.67 for $x = 0.0, 0.1, 0.15,$ and 0.2, respectively, shown in Table 2. Thus, optical band gap decrease with increasing Y concentration consistent with the earlier reported result by Antonio Perejon et al. [10]. This reduction in the band gap of all Y^{3+}-substituted BFO samples can be caused by the enhancement in the internal chemical pressure and reduced oxygen vacancies located at FeO_6 [29]. Also, the observed values of band gap are lower than earlier reported results of Y-substituted BFO nanoparticles [10, 30]. The observed value of microstrain and crystallite size influence significantly the band gap of BFO nanoparticles [31]. For sample $x = 0.2$, reduced value of particle size are responsible for disturbance in connectivity of FeO_6 octahedra throughout the unit cells and changes Fe-O-Fe length that may affect the intensity and position of energy bands . Thus, this can be attributed to the small value of band gap of the $x = 0.2$ sample. On the basis of these results, the developed nanoparticles can be considered appropriate for visible-light photocatalytic and solar cell applications.

Fig. 3 FESEM micrograph of $Bi_{1-x}Y_xFeO3$ ($x = 0.0, 0.1, 0.15, 0.2$) nanoparticles
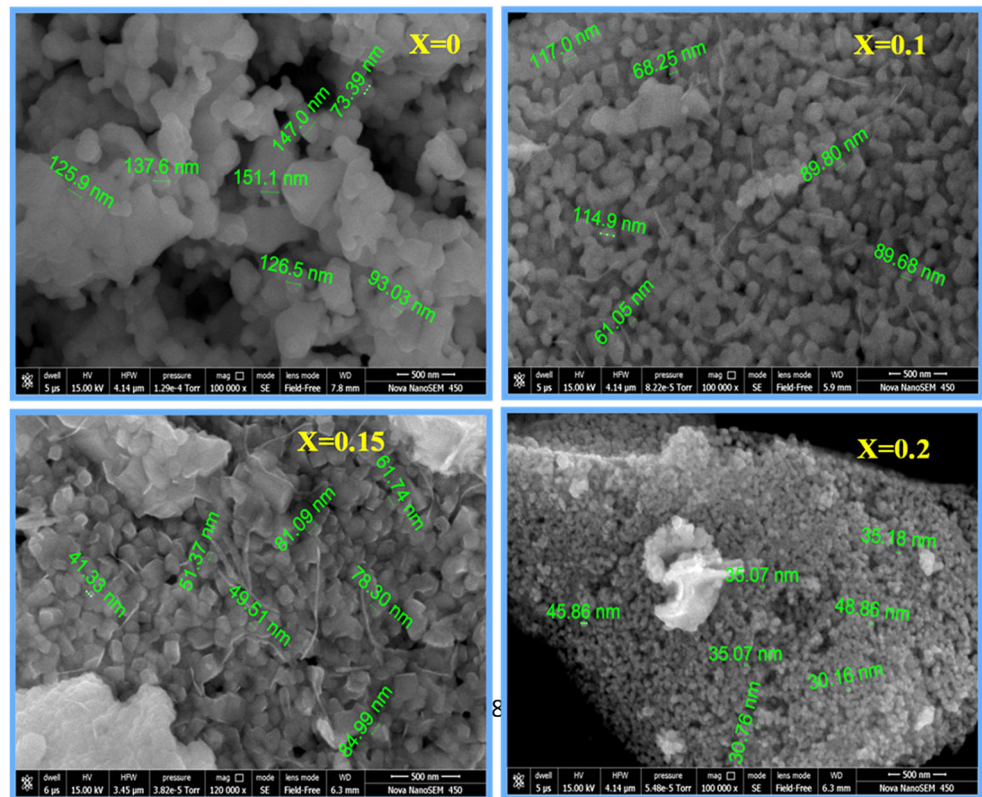
3.4 Magnetic Properties

Figure 6 explore the variation of magnetization with applied magnetic field (M-H) loop for $Bi_{1-x}Y_xFeO_3$ ($x = 0.0, 0.1, 0.15, 0.2$) nanoparticles. The observed loop of pristine BFO and Y-substituted samples having $x \leq 0.15$ show weak ferromagnetic behavior. The main observed characteristics obtained was superparamagnetic behavior of $x = 0.2$ sample having saturation magnetization value, $M_s = 1.33$ emu/g.

The observed value of saturation magnetization (M_s) are 0.23, 0.58, 0.78, and 1.33 emu/g and remnant magnetization (M_r) are 0.041, 0.113, 0.214, and 0.111 emu/g for $x = 0.0, 0.1, 0.15$, and 0.2, respectively, which is greater than earlier reported results [18, 32–34]. Also, the observed value of coercivity (H_c) are 180, 185, 221, and 37 gauss for $x = 0.0, 0.15, 0.1$, and 0.2, respectively, which is relatively lower than previously reported results [18, 32–34]. Thus, there is an increasing trend of coercivity observed with increasing Y concentration (up to $x = 0.15$) and exceptionally low value of coercivity for $x = 0.2$ is observed because of its small value of crystallite size (17 nm) as compared with all other compositions. And, as the smaller size particles are easy to demagnetize, so we get small value of coercivity for this composition.

BFO is a G-type antiferromagnetic ordering along the $[001]_{hex}$ axis in the hexagonal representation so basically, it should provide limited spontaneous magnetization. Nonetheless, a small magnetic moment is induced due to

partially broken antiferromagnetic ordering results from Dzyaloshinski-Morya interaction [35]. However, due to the rotation of this magnetic moment, a spin cycloid with wave vector along $[110]_{hex}$ axis having wavelength 64 nm is created [35]. Thus, disruption of spin-cycloid at length smaller than 64 nm can quench helicoidal order that produces weak ferromagnetism which is observed in our samples [36]. Overall, the materials having crystallites or particles size smaller than 60–70 nm are designate to quenching of entire spin-cycloid because of uncompensated spins of Fe^{3+} ions at the surface of particles [36]. Thus, a system of antiferromagnetic core superimposed with a ferromagnetic surface can be suggested on the basis of this theory for crystallite and particle size 60–70 nm. This assumption is in best agreement with the magnetic parameters of samples $x \leq 0.15$. But, sample $x = 0.2$ having crystallite size 17 nm develops a strong internal magnetization due to exchange coupling of electrons within the domain and thus becomes superparamagnetic. Exceptionally superparamagnetic behavior for $x = 0.2$ is observed because of smaller size of these particles. These particles thus show lower coercivity/retentivity and along with it these have significant magnetization values, so these can be considered in superparamagnetic category. Significant enhancement in the magnetization of $x = 0.2$ can also be attributed to the broken complete spin-cycloidal structure due to large number of uncompensated Fe^{3+} ions spins at the particle's surface, rather the reduction of spin-cycloid without breaking completely as
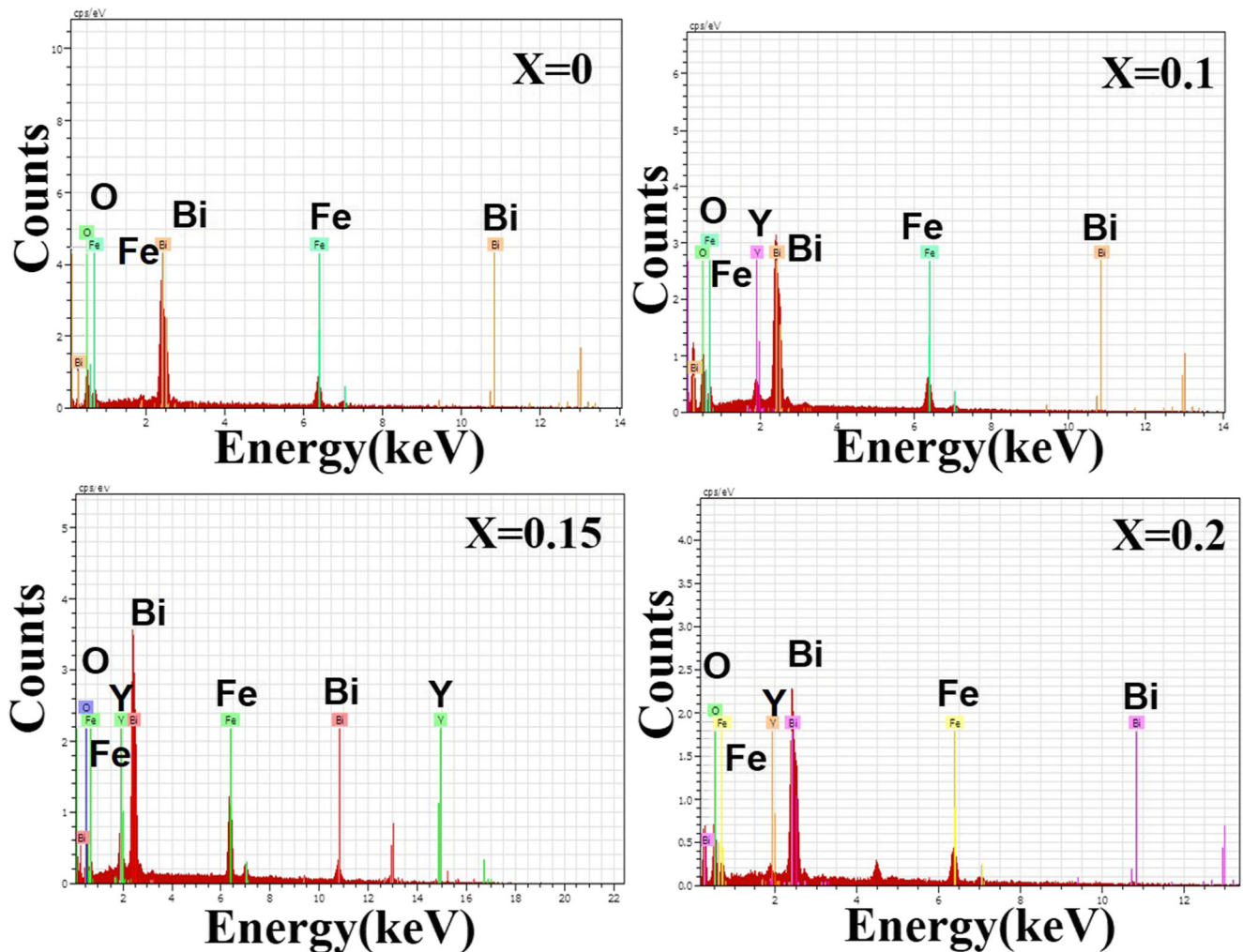
Fig. 4 EDS spectra of $Bi_{1-x}Y_xFeO_3$. **a** $x = 0.0$ nanoparticles. **b** $x = 0.1$ nanoparticles. **c** $x = 0.15$ nanoparticles. **d** $x = 0.2$ nanoparticles

for $x \leq 0.15$. Some other factors may also be responsible for the enhancement in magnetization such as (a) structural distortion which was significantly observed by XRD results for $x = 0.2$, spread throughout the particle, due to which fluctuation of magnetic moment can take place around the easy axis of magnetization [35] and (b) change in magnetic anisotropy which are tabulated in Table 2.

Additionally, the value of coercivity and saturation magnetization can be used to find the anisotropy field (H_K) tabulated in Table 2. This represents the indirect measurement of the crystal anisotropy forces and binds the magnetization in a favored direction. The equations used to calculate H_K are [37, 38]:

$$H_K = \frac{2K_1}{M_s} \qquad (5)$$

and

$$K_1 = \frac{M_s \times H_c}{0.98} \qquad (6)$$

where K_1 represents anisotropy constant, M_s is saturation magnetization, and H_c is coercivity . In the present results, there is a significant decrease in the value of H_K(in Table 2) for $x = 0.2$ which may also be the factor for the enhancement in magnetization of this composition.

3.5 Dielectric Measurements

The dielectric constant (ε_r) and dielectric loss (tanδ) (in inset) versus frequency (20 Hz to 2 MHz) plot for $Bi_{1-x}Y_xFeO_3$ ($x = 0.0, 0.1, 0.15, 0.2$) nanoparticles are depicted in Fig. 7. The dielectric constant is increasing with an increase in Y^{3+} concentration for $x = 0.1$ to 0.2. However, pristine BFO having a high value of dielectric constant than $x = 0.1$ to 0.15 and lower than $x = 0.2$ sample. All the samples exhibit decreasing behavior of dielectric constant and loss with increasing frequency up to 10 kHz and relatively become constant in the further frequency range (100 kHz to 2 MHz). This particular behavior perhaps explained on the ground of Wagner [39] and Maxwell [40] model of space charge polarization and is in accordance
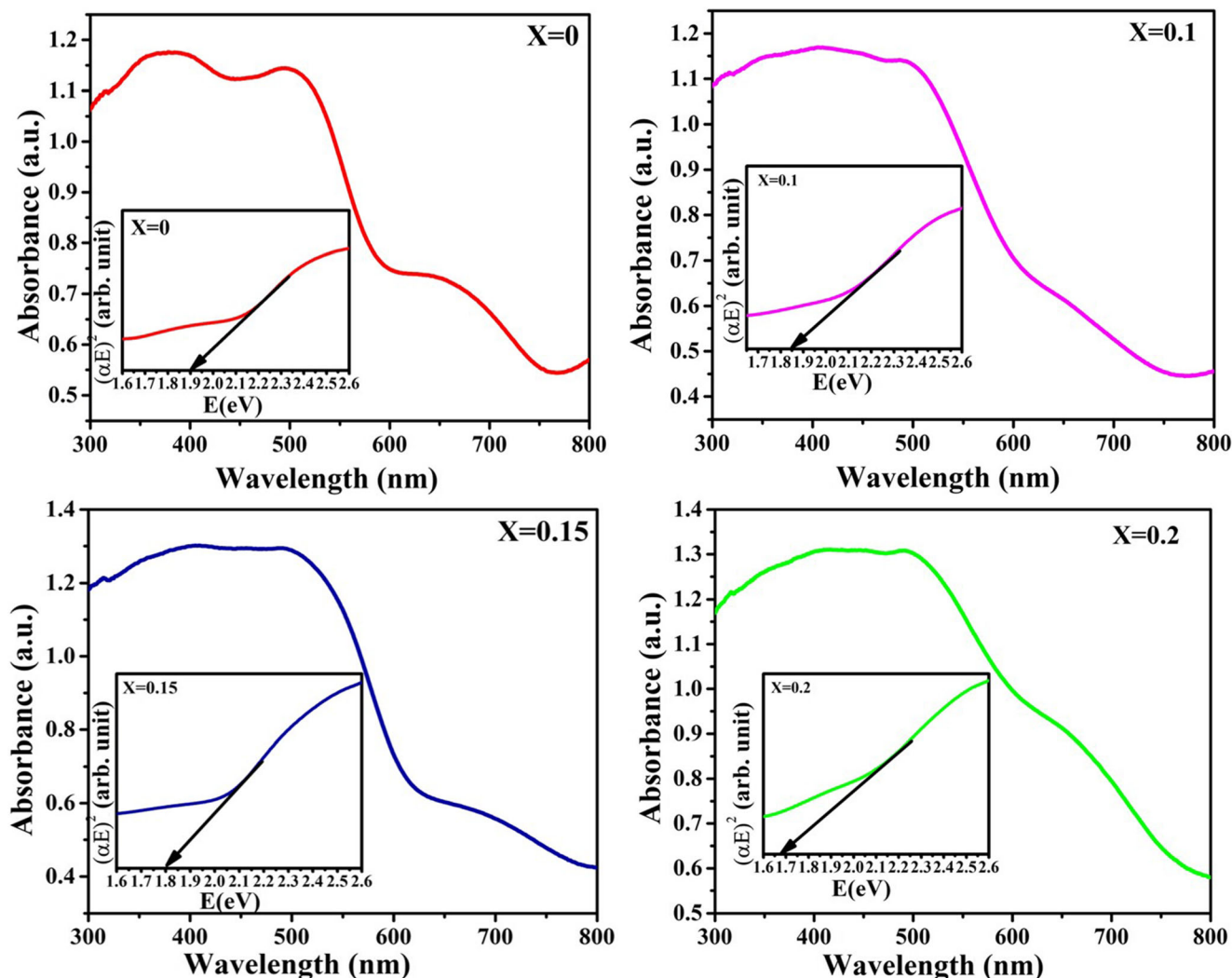
Fig. 5 Diffuse reflectance spectrum for $Bi_{1-x}Y_xFeO_3$ ($x = 0.0, 0.1, 0.15, 0.2$) nanoparticles and inset show band gap of respective composition calculated by Tauc's plot

with the Koop's phenomenological theory [41]. Most of the contribution to the dielectric constant in the low-frequency region carried out by the space charge emerge from vacancies due to oxygen and bismuth in the developed nanoparticles that are able to follow the applied electric field. In spite of it, in the high-frequency region, space charge does not get enough time to pursue a fast-growing field and go through relaxation.

Further, reduced oxygen vacancies due to Y doping (up to $x = 0.15$) may control this dispersion in both dielectric and loss pattern. Also, for $x = 0.2$, the highest value of dielectric constant is observed which may occur due to more dispersion in the obtained pattern. These enhanced dispersive characteristics originate due to the significant density of mobile charges and space charge polarization [42]. From Fig.7, the estimated value of dielectric constant at 20 Hz for samples $x = 0.0, 0.1, 0.15$, and 0.2 are 1015, 918, 937, and 1390, respectively.

Figure 8 represent the temperature-dependent dielectric constant (ε_r) and dielectric loss (tanδ) (inset) at 1 MHz frequency for $Bi_{1-x}Y_xFeO_3$ ($x = 0.0, 0.1, 0.15, 0.2$) nanoparticles. In dielectric constant (ε_r) and dielectric loss (tanδ) pattern, an anomaly around 380 °C, 400 °C, 390 °C, and 360 °C has been observed for samples $x = 0.0, 0.1, 0.15$, and 0.2, respectively. The observed anomaly around temperature range (360 to 400 °C) is in the proximity of antiferromagnetic Neel temperature of BFO [43, 44]. Also, this antiferromagnetic to
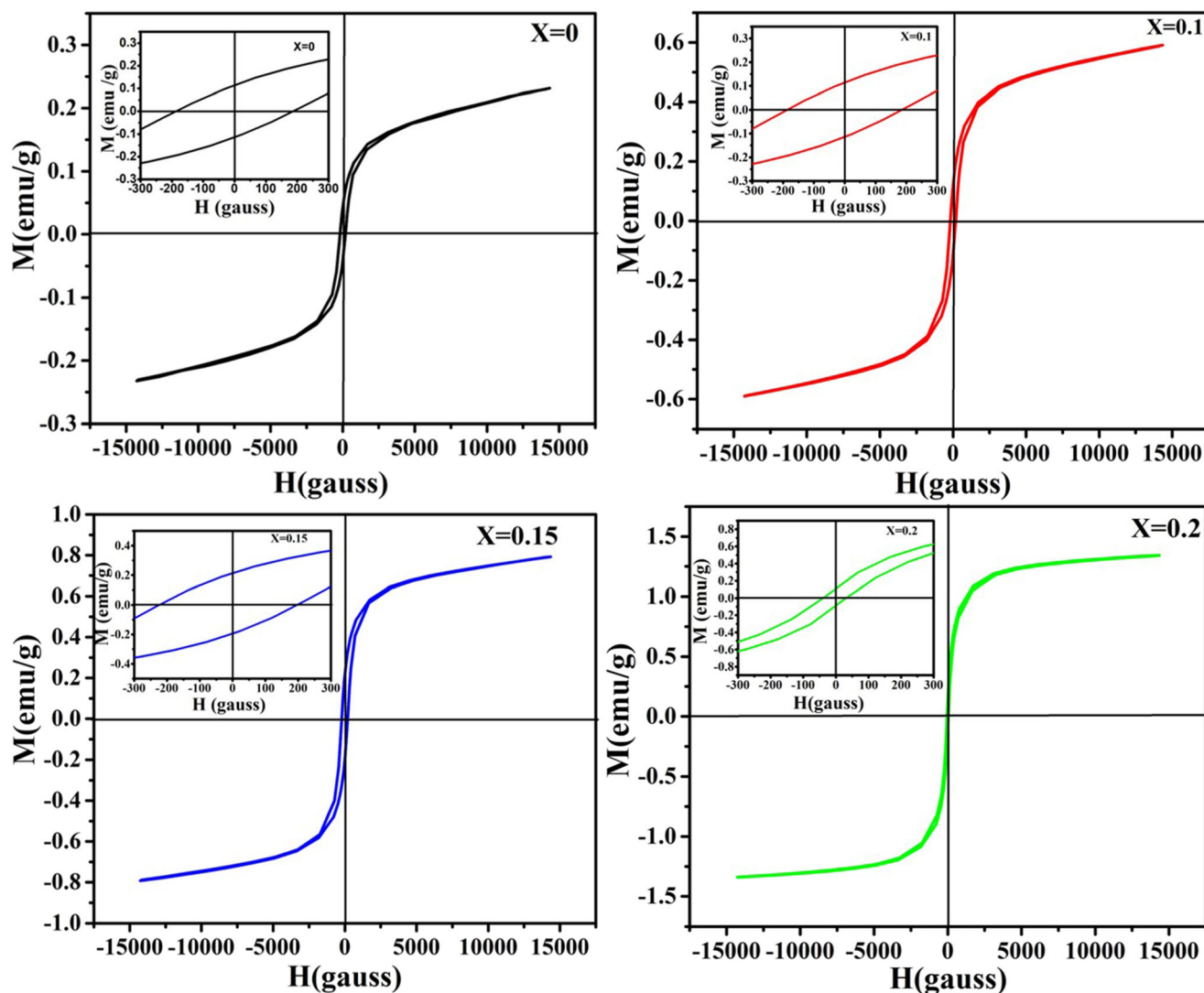
Table 2 Saturation magnetization (M_s), remanence magnetization (M_r), coercivity (H_c), anisotropy field (H_K), and optical band gap (E_g) of $Bi_{1-x}Y_xFeO_3$ ($x = 0.0, 0.1, 0.15, 0.2$) nanoparticles

Sample	M_s (emu/g)	M_r (emu/g)	H_c (gauss)	H_K (gauss)	E_g (eV)
$x = 0.0$	0.23	0.041	180	367.33	1.90
$x = 0.1$	0.58	0.113	185	377.55	1.85
$x = 0.15$	0.78	0.214	221	451.02	1.80
$x = 0.2$	1.33	0.111	37	75.50	1.67

Fig. 6 M-H loop of $Bi_{1-x}Y_xFeO_3$ ($x = 0.0, 0.1, 0.15, 0.2$) nanoparticles at room temperature

paramagnetic transition around 360 to 400 °C mainly occur due to the modification in spin structure which is coupled to ferroelectric ordering. Therefore, an anomaly around the above temperature range is observed in dielectric behavior [45]. Further, from literature, M-H loop of BFO nanoparticles at different temperature show weak ferromagnetic state in-between antiferro to paramagnetic state [46].

Additionally, superparamagnetic state always exists near the ferromagnetic state than the paramagnetic state and for sample $x = 0.2$, which is superparamagnetic at room temperature a strong internal magnetization from exchange coupling of electrons within the domain and weak magnetic exchange interaction in-between the domains will occur. This weak exchange interaction in-between the domain for sample $x = 0.2$ will be disrupted at lower temperature than other samples. Thus, for $x = 0.2$, anomaly temperature will decrease due to finite size effect and its superparamagnetic behavior. On the contrary, for sample $x = 0.1$ and 0.15, magnetic exchange

interaction in-between the domains is large as compared with the $x = 0.2$ sample; therefore, antiferromagnetic transition temperature will increase accordingly. Therefore, the anomaly temperature for $x = 0.1$ and 0.15 samples will be increased. Moreover, aforesaid anomaly in dielectric behavior has been anticipated by Landau-Devonshire phase transition theory in a magnetoelectrically structured arrangement. Thus, it reveals the indirect existence of magnetoelectric coupling in all samples by indicating magnetic order loss on electric order [47].

3.6 Electric Polarization and Strain Results Analysis

The polarization due to an electric field or P-E hysteresis loop and induced strain due to an applied electric field of value 15 kV/cm and frequency 50 Hz at room temperature for developed $Bi_{1-x}Y_xFeO_3$ ($x = 0.0, 0.1, 0.15, 0.2$) nanoparticles are shown in Figs. 9 and 10, respectively. In Fig. 9, the observed value of remnant polarization (P_r) is increased with increasing
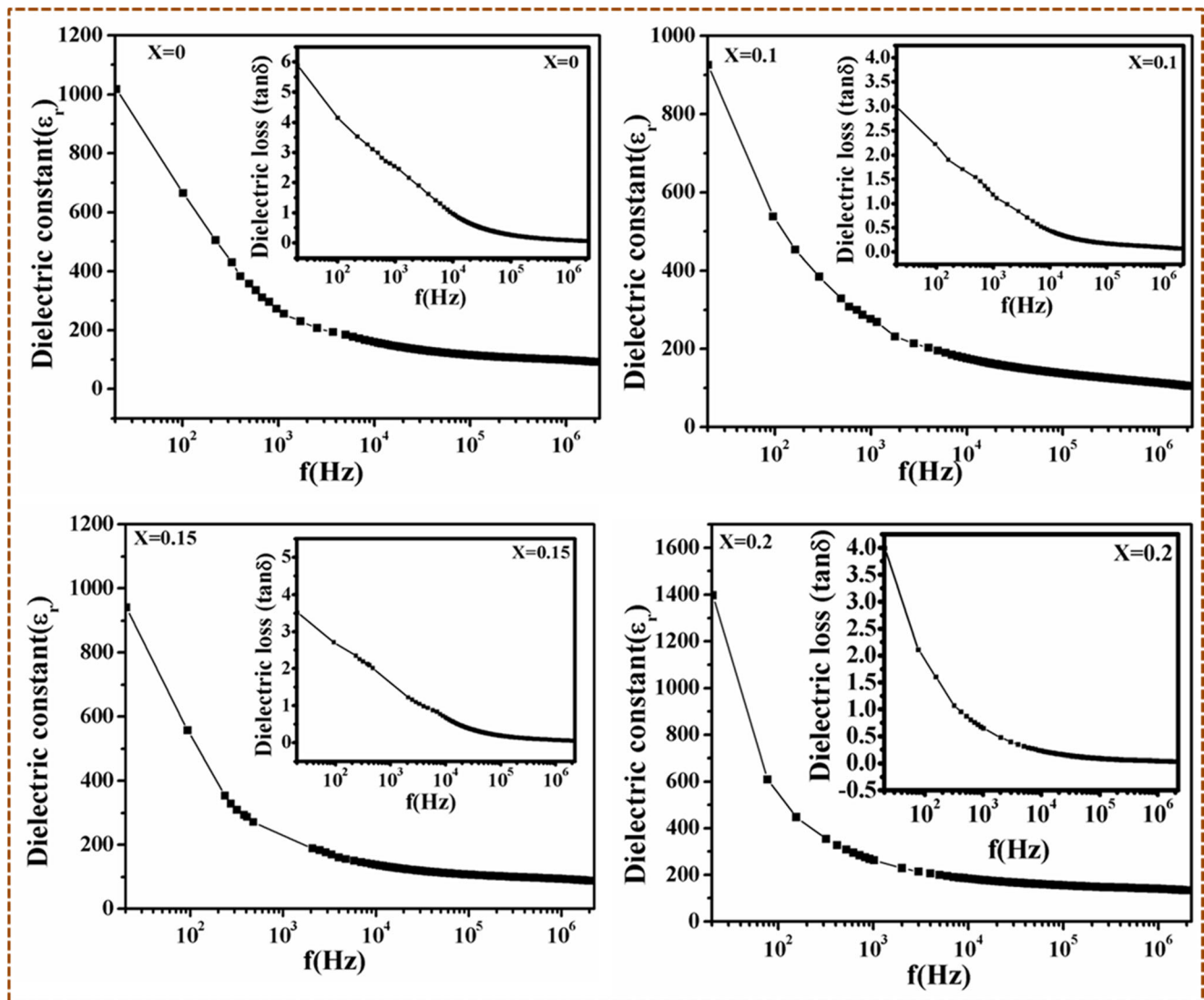
Fig. 7 Dielectric constant versus frequency of $Bi_{1-x}Y_xFeO_3$ ($x = 0.0, 0.1, 0.15, 0.2$) nanoparticles and inset show their respective dielectric loss versus frequency variation at room temperature

concentration of Y^{3+} which are 0.16, 1.29, 11.7, and 15.90 for $x = 0.0, 0.1, 0.15,$ and 0.2 samples, respectively. Also the value of coercive field (E_c) first increases up to $x = 0.15$ and then decrease for the $x = 0.2$ sample and the values are 10.84, 13.70, 14.66, and 12.40 for $x = 0.0, 0.1, 0.15,$ and 0.2 composition, respectively. Pristine BFO exhibit unsaturated P-E loop which may arise due to oxygen vacancies that create feasible leakage current and make it conducting in nature [11, 48]. Other possible defects dipoles in BFO may also responsible for such type of unsaturated behavior in the P-E loop. Although these loops show unsaturated behavior, but the values of maximum polarization, retentivity, and coercivity are increasing with substitution of yttrium which are tabulated in Table 3. Further, Y-substituted samples display penning of P-E loop which represents the resistive nature of these samples [49, 50]. P-E loop of all the samples exhibit penning of loops and unsaturation behavior because of lower value of electric

field. Moreover, reduced oxygen vacancies due to substitution of Y^{3+} in BFO and diminish charge defect by virtue of resistive nature are responsible for less leakage current in the $x = 0.1$ and 0.15 samples. Structure transformation also plays an important factor for the enhancement in polarization, therefore $x = 0.2$ sample exhibit less penning of loop than other Y-substituted samples due to significant density of mobile charges and space charge polarization [49].

Thus, we observe improved ferroelectric property as a result of enhancement in the polarization of all Y^{3+} substituted BFO samples as shown in Table 3.

Additionally, the electric field–induced strain (S) can be estimated by [51]:

$$S = QP^2 \tag{7}$$

where Q is the electrostrictive constant and P is

Fig. 8 Variation of dielectric constant with temperature at 1 MHz of $Bi_{1-x}Y_xFeO_3$ ($x = 0.0$, 0.1, 0.15, 0.2) nanoparticles and inset show their respective dielectric loss vs. temperature variation
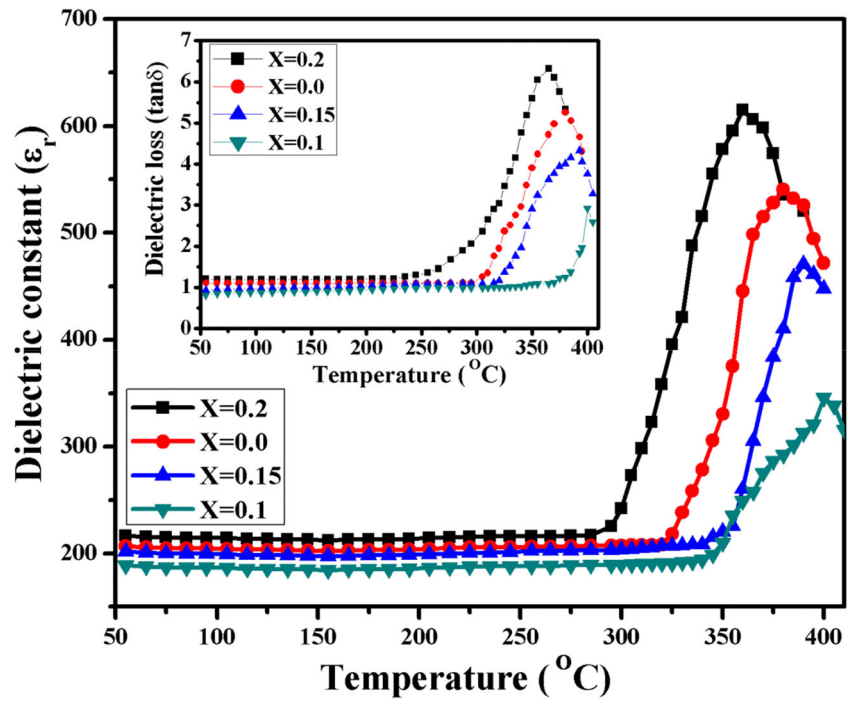
polarization. Such behavior is generally related to switching and movement of domains due to the electric field that may involve a significant variation in the configuration of the grains [52]. In Fig.10, pristine BFO
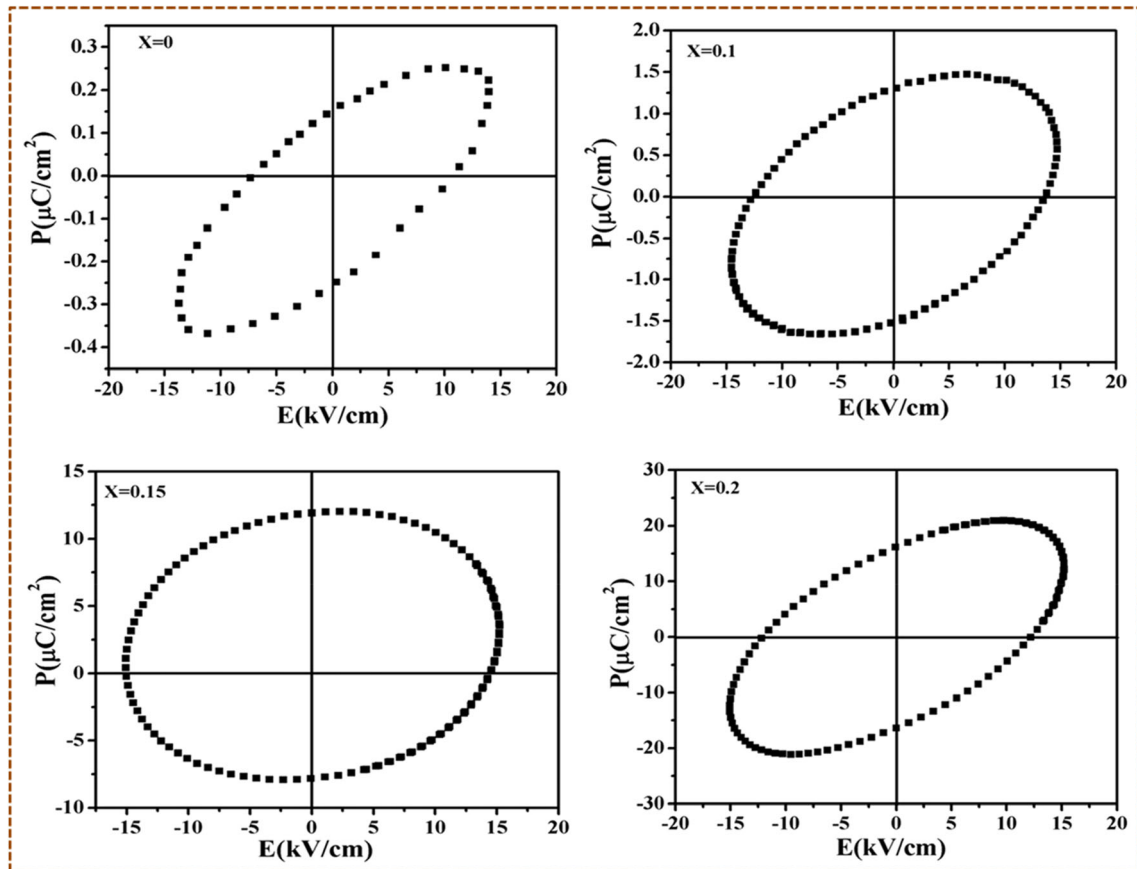

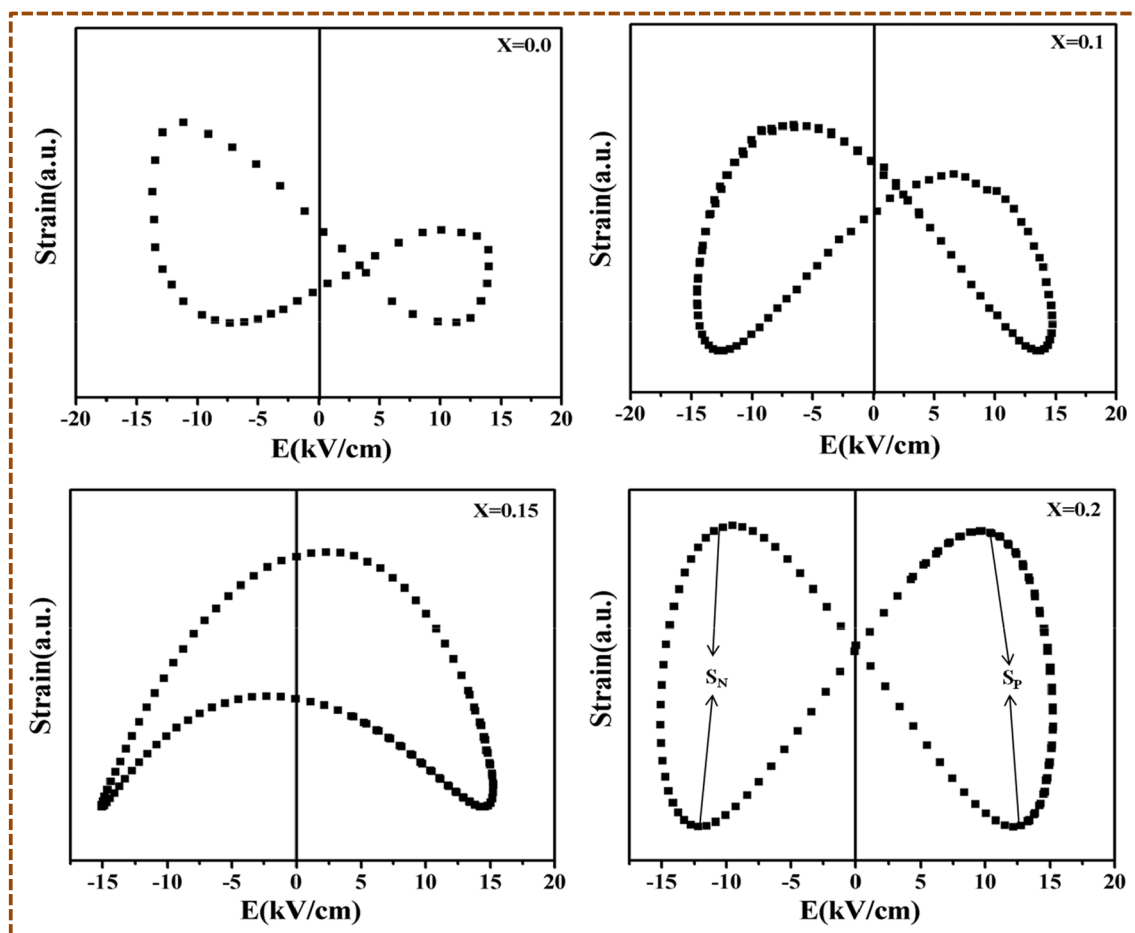**Fig. 9** Room temperature P-E loop of $Bi_{1-x}Y_xFeO_3$ ($x = 0.0$, 0.1, 0.15, 0.2) nanoparticles

Fig. 10 Room temperature S-E loop of $Bi_{1-x}Y_xFeO_3$ ($x = 0.0, 0.1, 0.15, 0.2$) nanoparticles

represent asymmetric behavior which may be caused by the presence of different dipole defects [53]. Doping of Y^{3+} reduces the asymmetric factor and highest substituted sample ($x = 0.2$) show more symmetrical loop which looks a like typical butterfly shape. Thus, we observe the highest value of S_P (peak to peak strain value in the positive wing) and S_N (peak to peak strain value in the negative wing) for $x = 0.2$ sample (shown by an arrow in Fig.10) which may be due to more active switching of domains [49]. Also, S-E loop depicted in Fig. 10 is unsaturated which illustrate the variation of S_P and S_N are not in particular appearances for all the samples. There can be little influence of the minor amount of impurity

Table 3 Maximum polarization (P_m), remnant polarization (P_r), and coercivity (E_c) of $Bi_{1-x}Y_xFeO_3$ ($x = 0.0, 0.1, 0.15, 0.2$) nanoparticles

Sample	P_m ($\mu c/cm^2$)	P_r ($\mu c/cm^2$)	E_c (kV/cm)
$x = 0.0$	0.25	0.16	2.73
$x = 0.1$	1.49	1.32	13.54
$x = 0.15$	12.03	12.03	14.56
$x = 0.2$	21.15	16	12.81

phases on large strain value.

4 Conclusion

In summary, $Bi_{1-x}Y_xFeO_3$ ($x = 0.0, 0.1, 0.15, 0.2$) nanoparticles were developed via sol-gel auto-combustion route. XRD pattern analyzed small crystal structure distortion due to Y^{3+} doping with the exception of $x = 0.2$ which show large structure distortion. FESEM micrograph revealed inhibition of grain growth and enhancement in the homogeneity of BFO due to Y^{3+} doping. EDS spectra clearly demonstrate the existence of precondition compositions in all the samples. The optical band gap decreases with increasing doping concentration due to enhancement in the internal chemical pressure, thus making it a suitable material for photovoltaic and photocatalytic applications. The room temperature magnetic measurements show remarkable superparamagnetic behavior for $x = 0.2$ and also exhibit increasing trend of magnetization with increasing Y^{3+} concentration. All the samples exhibit decreasing behavior of dielectric constant in the lower frequency region and become almost constant in the upper frequency range. Also, sample $x = 0.2$ show maximum value of dielectric

constant due to its significant density of space charge polarization by virtue of its small grain size. Temperature-dependent dielectric constant and loss reveal an abnormality in the temperature range 370 to 410 °C as a consequence of indirect magnetoelectric coupling. The room temperature P-E hysteresis loop represent improvement in ferroelectric properties with increasing Y^{3+} concentration and also obtained electric field strain using polarization values. The peak to peak strain values for the right (S_P) and left (S_N) wing is observed maximum for $x = 0.2$ which can be attributed to more active switching of the domain.

References

1. Jiang, Q.H., Nan, C.W., Shen, Z.J.: J. Am. Ceram. Soc. **89**, 2123 (2006)
2. Wang, Y.P., Zhou, L., Zhang, M.F., Chen, X.Y., Liu, J.M., Liu, Z.G.: Appl. Phys. Lett. **84**, 1731 (2004)
3. Wang, J., Neaton, J.B., Zheng, H., Nagarajan, V., Ogale, S.B., Liu, B., Viehland, D., Vaithyanathan, V., Schlom, D.G., Waghmare, U.V., Spaldin, N.A., Rabe, K.M., Wuttig, M., Ramesh, R.: Science. **299**, 1719 (2003)
4. Fiebig, M., Lottermoser, T., Frohlich, D., Goltsev, A.V., Pisarev, R.V.: Nature. **419**, 818 (2002)
5. Gavriliuk, A.G., StruzhkinI, V.V., LyubutinI, S., Troyanet, A.: JETP Lett. **86**, 197 (2007)
6. Banerjee, M., Mukherjee, A., Banerjee, A., Das, D., Basu, S.: N. J. Chem. **41**, 10985 (2017)
7. Catalan, G., Scott, J.F.: Adv. Mater. **21**, 2463 (2009)
8. Chauhan, S., Arora, M., Sati, P.C., Chhoker, S., Katyal, S.C., Kumar, M.: Ceram. Int. **39**, 6399 (2013)
9. Takahashi, K., Kida, N., Tonouchi, M.: Phys. Rev. Lett. **96**, 1 (2006)
10. Fkia, H., Koubaaa, M., Sicardb, L., Cheikhrouhou-Koubaaa, W., Cheikhrouhoua, A., Ammar-Merahb, S.: Ceram. Int. **43**, 4139 (2017)
11. Eerenstein, W., Mathur, N.D., Scott, J.F.: Nature. **442**, 759 (2006)
12. Azough, F., Freer, R., Thrall, M., Cernik, R.J., Tuna, F., Collison, D.: J. Eur.Ceram. Soc. **30**, 727 (2010)
13. Yu, B., Li, M., Liu, J., Guo, D., Pei, L., Zhao, X.: J. Phys. Appl. Phys. **41**, 065003 (2008)
14. Das, S.R., Choudhary, R.N.P., Bhattacharya, P., Katiyara, R.S.: J. Appl. Phys. **101**, 034104 (2007)
15. Layek, S., Verma, H.C., Garg, A.: J. Alloy. Compd. **651**, 294–301 (2015)
16. Ramachandran, B., Dixit, A., Naik, R., Lawes, G., Ramachandra Rao, M.S.: J. Appl. Phys. **111**, 023910 (2012)
17. Mao, W., Wang, X., Han, Y., Li, X., Li, Y., Wang, Y., Ma, Y., Feng, X., Yang, T., Yang, J., Huang, W.: J. Alloy. Compd. **584**, 520–523 (2014)
18. Medina, L.M.S., Jorge, G.A., Negri, R.M.: J. Alloy. Compd. **592**, 306 (2014)
19. Mishra, R.K., Pradhan, D.K., Choudhary, R.N.P., Banerjee, A.: J. Phys. Condens. Matter. **20**, 045218 (2008)
20. Gautam, A., Uniyal, P., Yadav, K.L., Rangra, V.S.: J. Phy. Chemist. Solid. **73**, 188 (2012)
21. Zhong, M., Kumar, N.P., Sagar, E., Jian, Z., Yemin, H., Reddy, P.V.: Mater. Chem. Phys. **173**, 126 (2016)
22. Gore, S.K., Mane, R.S., Naushad, M., Jadhav, S.S., Zate, M.K., Alothman, Z.A., Hui, B.K.N.: Dalt. Trans. **44**, 6384 (2015)
23. Singh, A., Singh, V., Bamzai, K.K.: Mater. Chem. Phys. **155**, 92 (2015)
24. Karimi, S., Reaney, I.M., Levin, I., Sterianou, I.: Appl.Phys.Lett. **94**, 112903 (2009)
25. Verma, V., Beniwal, A., Ohlan, A., Tripathi, R.: J. Mag. Mag. **394**, 385 (2015)
26. Gao, F., Chen, X.Y., Yin, K.B., Dong, S., Ren, Z.F., Yuan, F., Yu, T., Zou, Z., Liu, J.M.: Adv. Mater. **19**, 2889 (2007)
27. Tauc, J., Grigorovici, R., Vancu, A.: Phys. Stat. Solid. B. **15**, 627 (1966)
28. Ihlefeld, J.F., Podraza, N.J., Liu, Z.K., Rai, R.C., Xu, X., Heeg, T., Chen, Y.B., Li, J., Collins, R.W., Musfeldt, J.L., Pan, X.Q., Schubert, J., Ramesh, R., Schlom, D.G.: Appl. Phys. Lett. **92**, 142908 (2008)
29. Arora, M., Kumar, M.: Mater. Lett. **137**, 285 (2014)
30. Bellakki, M.B., Manivannan, V.J.: Sol-Gel Sci. Technol. **53**, 184 (2010)
31. Mocherla, P.S.V., Karthik, C., Ubic, R., Ramachandra Rao, M.S., Sudakar, C.: Appl. Phy. Lett. **103**, 022910 (2013)
32. Zhanga, Y.S.X., Wanga, X., Wangc, Y., Wanga, Z.: J. Alloys. Comp. **507**, 157 (2010)
33. Nalwa, K.S., Garg, A., Upadhyaya, A.: Mater. Lett. **62**, 878 (2008)
34. Luo, L., Shen, K., Xu, Q., Zhou, Q., Wei, W., Gondal, M.A.: J. Alloys. Comp. **558**, 73 (2013)
35. Park, T.J., Papaefthymiou, G.C., Viescas, A.J., Moodenbaugh, A.R., Wong, S.S.: Nano Lett. **7**, 766 (2007)
36. Ederer, C., Spaldin, N.A.: Phys. Rev. B. **71**, 060401 (2005)
37. Humbe, A.V., Kounsalye, J.S., Shisode, M.V., Jadhav, K.: Ceram. Int. **44**, 5466 (2018)
38. Trukhanov, S., Trukhanov, A., Vasiliev, A., Balagurov, A., Szymczak, H.: J. Exp. Theor. Phys. **113**, 819 (2011)
39. Wagner, K.W.: Zur theorie der unvollkommenen dielektrika. Ann.Phys.(Leipzig). **40**(817), (1913)
40. Maxwell, J.C.: Electricity and Magnetism, vol. vol.1. Oxford University Press, Oxford (Section328 (1929)
41. Koops, C.G.: Phys. Rev. **83**(1), 121 (1951)
42. Jonscher, A.K., Meca, F., Millany, H.M.: J.Phys. C: Solid State Phys. **12**, L293 (1979)
43. Das, A., De, S., Bandyopadhyay, S., Chatterjee, S., Das, D.: J. Alloys Compd. **697**, 353 (2017)
44. Sheoran, N., Kumar, V., Kumar, A.: J. magnet. and magnet. mater. **475**, 30 (2019)
45. Godara, S., Sinha, N., Ray, G., Kumar, B.: J. Asia. Ceram. Society. **2**, 421 (2014)
46. Lin, J.W., Tang, Y.H., Lue, C.S., Lin, J.G.: Appl. Phy. Lett. **96**, 232507 (2010)
47. Kimura, T., Kawamoto, S., Yamada, I., Azuma, M., Takno, M., Tokura, Y.: Phys. Rev.B. **67**, 180401 (2003)
48. Arya, G.S., Kotnala, R.K., Negi, N.S.: J. Appl. Phys. **113**, 044107 (2013)
49. Kumar, P., Chand, P.: J. Allo. and Comp. **748**, 504 (2018)
50. Arlt, G.: Ferroelectrics. **104**, 217 (1990)
51. Wang, K., Yao, F.Z., Jo, W., Gobeljic, D., Shvartsman, V.V., Lupascu, D.C., Li, J.F., Rödel, J.: Adv. Funct. Mater. **23**, 4079 (2013)
52. Rojac, T., Kosec, M., Damjanovic, D.: J. Am. Ceram. Soc. **94**, 4108 (2011)
53. Eric Cross, L.: Ferroelectrics. **76**, 241 (1987)